

# Multi-Base Station Cooperative Sensing with AI-Aided Tracking

Elia Favarelli, Elisabetta Matricardi, Lorenzo Pucci, Enrico Paolini, Wen Xu, Andrea Giorgetti

**Abstract**—In this work, we investigate the performance of a joint sensing and communication (JSC) network consisting of multiple base stations (BSs) that cooperate through a fusion center (FC) to exchange information about the sensed environment while concurrently establishing communication links with a set of user equipments (UEs). Each BS within the network operates as a monostatic radar system, enabling comprehensive scanning of the monitored area and generating range-angle maps that provide information regarding the position of a group of heterogeneous objects. The acquired maps are subsequently fused in the FC. Then, a convolutional neural network (CNN) is employed to infer the category of the targets, e.g., pedestrians or vehicles, and such information is exploited by an adaptive clustering algorithm to group the detections originating from the same target more effectively. Finally, two multi-target tracking algorithms, the probability hypothesis density (PHD) filter and multi-Bernoulli mixture (MBM) filter, are applied to estimate the state of the targets. Numerical results demonstrated that our framework could provide remarkable sensing performance, achieving an optimal sub-pattern assignment (OSPA) less than 60 cm, while keeping communication services to UEs with a reduction of the communication capacity in the order of 10% to 20%. The impact of the number of BSs engaged in sensing is also examined, and we show that in the specific case study, 3 BSs ensure a localization error below 1 m.

**Index Terms**—joint sensing and communication, tracking, orthogonal frequency division multiplexing, millimeter-wave, artificial intelligence, convolutional neural network

## I. INTRODUCTION

THE forthcoming generation of mobile radio networks is poised to offer a range of emerging functionalities, including innovative services. Notably, the ability to perform effective sensing using radio frequency (RF) signals has become feasible due to the evolution toward larger antenna arrays, namely massive multiple-input multiple-output (mMIMO), and higher frequency bands [1], [2]. The joint sensing and communication (JSC) approach leverages existing communication infrastructure to provide sensing capabilities, offering advantages such as reduced costs and improved spectral and energy efficiency when compared to dedicated spectrum- and transceiver-dependent systems like radar [3]. This convergence of sensing and communication systems envisioned for future

This work was supported by the CNIT National Laboratory WiLab and the WiLab-Huawei Joint Innovation Center.

Elia Favarelli, Elisabetta Matricardi, Lorenzo Pucci, Enrico Paolini, and Andrea Giorgetti are with the Department of Electrical, Electronic, and Information Engineering “Guglielmo Marconi” (DEI), University of Bologna, and the Wireless Communications Laboratory (WiLab), CNIT, Italy (e-mail: {elia.favarelli, elisabetta.matricardi3, lorenzo.pucci3, e.paolini, andrea.giorgetti}@unibo.it).

Wen Xu is with Munich Research Center, Huawei Technologies Duesseldorf GmbH, Munich, Germany, (email: wen.dr.xu@huawei.com).

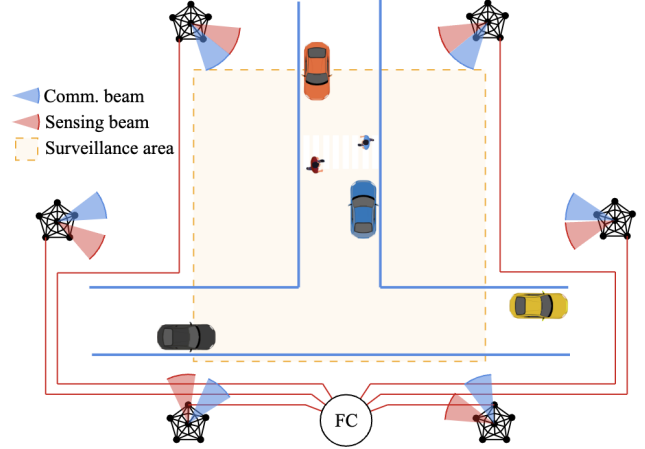


Figure 1: An urban scenario with 6 monostatic JSC base stations (BSs) aiming at monitoring pedestrians (point-like targets) and vehicles (extended targets) in a surveillance area. BSs communicate with their user equipments (UEs) while simultaneously sensing the surrounding environment via dedicated sensing beams. The fusion center (FC) collects measurements from the BSs via the backhaul network, fuses them to create likelihood maps, and performs detection, target identification, and multiple target tracking.

networks will enable ubiquitous sensing services that rely on capturing reflections from non-collaborative objects, thus playing a critical role, e.g., in intelligent vehicular networks [4]. Furthermore, the growing interest in sensing stems from its potential to support various applications, such as traffic monitoring, autonomous driving, safety in industrial environments, and environmental mapping [5], [6].

The advent of mMIMO technology in millimeter-wave (mmWave) bands facilitates the detection, tracking, and precise localization of pedestrians, vehicles, drones, and other moving objects in real-time scenarios [7]. This enables the acquisition of range profiles of targets, a kind of target fingerprint, as scatterers in complex objects may be resolved into different range cells. At the same time, the enormous advancement of artificial intelligence (AI), and particularly image identification, has generated a vast and solid portfolio of solutions that could also be exploited in the field of integrated sensing and communication (ISAC) [8]–[10].

This work aims to investigate the possibility of using multi-sensor fusion techniques combined with multi-target tracking algorithms, to exploit range-angle radar maps obtained through a set of cooperating BSs with monostatic sensing capability and orthogonal frequency division multiplexing (OFDM) signals. The main contributions can be summarized as follows:

- We propose a soft map fusion strategy based on range-angle maps obtained at each BS.

- We present an AI-based approach to infer the target category that is then exploited by an adaptive clustering methodology capable of managing point-like and extended targets.
- The adaptive clustering is then combined with tracking algorithms to perform target state estimation and prediction. Two different tracking algorithms, the probability hypothesis density (PHD) and multi-Bernoulli mixture (MBM) filter, are compared.
- We propose the optimal sub-pattern assignment (OSPA) metric and aggregate downlink capacity to evaluate the sensing and communication capabilities.
- Finally, we investigate the impact of the number of cooperative BSs performing sensing on the localization and communication performance.

In this work, capital and lowercase boldface letters represent matrices and vectors, respectively;  $\mathbf{D}_{q,t}$  stands for a matrix dependent on indexes  $q$  and  $t$ , while  $\mathbf{v}_{t,p}$  represents the  $p$ th column selected by the matrix  $\mathbf{V}_t$ .  $\mathbf{I}_n$  is the  $n \times n$  identity matrix;  $\|\cdot\|_p$  stands for the  $p$ -norm;  $|\cdot|$  represents the cardinality of a set;  $\delta(\cdot)$  is the Dirac delta function;  $\lfloor \cdot \rfloor$  represents the round operator;  $(\cdot)^c$  stands for conjugate;  $\mathbf{x} \sim \mathcal{CN}(\mathbf{0}, \mathbf{\Sigma})$  denotes a zero-mean circularly symmetric complex Gaussian random vector with covariance  $\mathbf{\Sigma}$ ; and  $\mathbf{x} \sim \mathcal{N}(\boldsymbol{\mu}, \mathbf{\Sigma})$  denotes the real-valued Gaussian random vector with mean  $\boldsymbol{\mu}$  and covariance  $\mathbf{\Sigma}$ .

The rest of the paper is organized as follows. Section II presents the JSC model. Section III describes the data fusion strategy, target identification methodology, clustering scheme, and tracking algorithms. System performance is evaluated in Section IV, and conclusions are drawn in Section V.

## II. SYSTEM MODEL

This work considers a JSC network, and a scenario, like the one portrayed in Figure 1. In particular, the considered system consists of several monostatic JSC BSs transmitting OFDM signals at mmWave using mMIMO technology. Each of these BSs is connected to an FC via backhaul; the FC allows them to cooperate in performing the detection and tracking of targets in the surveillance area. As shown later, the sensing task is accomplished through range-Doppler maps that each BS can generate by scanning the environment using a dedicated sensing beam. Moreover, to ensure communication functionality, each BS scans the environment for sensing and communicates with UEs in its respective cell using the same time-frequency resources via multiple beams. To keep interference among the sensing beams of different BSs at a negligible level, we consider the proper use of frequency division (FD) or time division (TD) through coordination.

Each monostatic BS is equipped with two separate uniform linear arrays (ULAs), one for transmission and one for reception, with  $N_T$  and  $N_R$  antennas respectively, and both with a half-wavelength separation between the elements. In particular, the transmitted waveform is used for communication and sensing, while the sensing receiver (Rx) only collects backscattered signals. More specifically, considering the downlink communication toward UEs, each BS transmits

frames consisting of  $M$  OFDM symbols and  $K$  subcarriers, and the same signals are simultaneously used to sense the environment. A multi-beam radiation pattern is used to split the power between sensing and communication by exploiting spatial diversity, as explained later. In particular, each BS uses a communication beam for the UE while steering a sensing beam scanning the environment within the angular interval  $[-\Theta_0, \Theta_0]$  with steps  $\Delta\Theta$ . In each sensing direction, a subset  $M_s < M$  of OFDM symbols is collected by the Rx.

The OFDM time-frequency grid containing the transmitted (complex) symbol for each sensing direction can be represented by a matrix  $\mathbf{X}_s \in \mathbb{C}^{K \times M_s}$  with elements  $x_k^{(m)}$ , where  $k$  is the subcarrier index and  $m$  is the OFDM symbol (or time) index.

Starting from this grid, a precoding operation is performed on its elements with the beamformer  $\mathbf{w}_T \in \mathbb{C}^{N_T \times 1}$  to map each complex symbol to each antenna and obtain the vector of the transmitted symbols  $\tilde{\mathbf{x}}_k^{(m)} = \mathbf{w}_T x_k^{(m)}$ . As previously mentioned, a multi-beam radiation pattern is considered at the Tx to split the total available power between the communication and sensing directions. Hence, the beamforming vector  $\mathbf{w}_T$  is defined as follows

$$\mathbf{w}_T = \frac{\sqrt{P_T G_T^a}}{N_T} (\sqrt{\rho_P} \mathbf{a}_T^c(\theta_{T,s}) + \sqrt{1 - \rho_P} \mathbf{a}_T^c(\theta_{T,c})) \quad (1)$$

where  $\rho_P \in [0, 1]$  is the fraction of power reserved for the sensing beam,  $P_T$  is the transmit power,  $G_T^a$  is the transmit array gain along the beam steering direction, and  $\mathbf{a}_T(\theta_{T,c}) \in \mathbb{C}^{N_T \times 1}$  and  $\mathbf{a}_T(\theta_{T,s}) \in \mathbb{C}^{N_T \times 1}$  are the steering vectors associated with the communication and sensing directions, respectively, being  $\theta_{T,c}$  and  $\theta_{T,s}$  the respective direction of departures (DoDs).

Starting from the vector of the transmitted symbols  $\tilde{\mathbf{x}}_k^{(m)}$ , the vector  $\tilde{\mathbf{y}}_k^{(m)} \in \mathbb{C}^{N_R \times 1}$  of symbols received at each antenna, after OFDM demodulation, is given by

$$\tilde{\mathbf{y}}_k^{(m)} = \mathbf{H}_k^{(m)} \tilde{\mathbf{x}}_k^{(m)} + \tilde{\mathbf{n}}_k \quad (2)$$

where  $\mathbf{H}_k^{(m)} \in \mathbb{C}^{N_R \times N_T}$  is the channel matrix for the  $m$ th symbol and the  $k$ th subcarrier, which will be defined later, and  $\tilde{\mathbf{n}}_k \sim \mathcal{CN}(\mathbf{0}, \sigma_N^2 \mathbf{I}_{N_R})$  is the noise vector.<sup>1</sup>

Spatial combining is then performed in the considered sensing direction,  $\theta_{R,s} = \theta_{T,s}$ , by using the receiving beamforming vector  $\mathbf{w}_R = \mathbf{a}_R^c(\theta_{R,s})$ . This yields the grid of the received symbols  $\mathbf{Y}_s \in \mathbb{C}^{K \times M_s}$ , whose  $(k, m)$  elements are defined as  $y_k^{(m)} = \mathbf{w}_R^T \tilde{\mathbf{y}}_k^{(m)}$ . The received symbols grid collected in each sensing direction is then used to generate range-angle maps, as explained in Section II-B.

### A. Target Models

This work considers both point-like targets, such as pedestrians, and extended targets, such as vehicles. Specifically, vehicles are represented by a model comprising 12 reflection points. These include 4 points to capture planar reflections originating from the front, back, and sides of the vehicle (characterized by a narrow visibility function and a substantial radar

<sup>1</sup>Both inter-carrier interference (ICI) and inter-symbol interference (ISI) are considered negligible.

Table I: Average RCS for different point reflections

Reflection	$\bar{\sigma}_{\text{rcs}} [\text{m}^2]$
Pedestrian	1
Surfaces	20
Wheelhouses	0
Corners	5

cross-section (RCS)), 4 points to account for the wheelhouses, and 4 points to simulate the corners [11]–[13].

Now, considering  $L$  as the total number of reflections from both extended and point-like targets, the channel matrix already introduced in Equation (2) is given by

$$\mathbf{H}_k^{(m)} = \sum_{l=1}^L \beta_l e^{j2\pi m T_s f_{D,l}} e^{-j2\pi k \Delta f \tau_l} \mathbf{a}_R(\theta_l) \mathbf{a}_T^T(\theta_l) \quad (3)$$

where  $\Delta f = 1/T$  is the subcarrier spacing,  $T_s = T + T_{\text{cp}}$  is the total OFDM symbol duration including the cyclic prefix time  $T_{\text{cp}}$ . Additionally,  $f_{D,l}$  refers to the Doppler shift,  $\tau_l$  represents the round-trip delay,  $\theta_l$  denotes the direction of arrival (DoA), and  $\mathbf{a}_R(\theta_l)$  represents the array response vector at the Rx for the  $l$ th backscattered signal. The complex term  $\beta_l = |\beta_l| e^{j\phi_l}$  includes phase shift and attenuation along the  $l$ th propagation path. The signal-to-noise ratio (SNR) at each receiving antenna related to the  $l$ th reflection point (hence the sensing SNR) becomes

$$\begin{aligned} \text{SNR}_l^{(s)} &= \rho_p \cdot \gamma_l \cdot \frac{P_T G_T^a G_R}{\sigma_N^2} |\beta_l|^2 \\ &= \rho_p \cdot \gamma_l \cdot \frac{P_T G_T^a G_R}{N_0 K \Delta f} \frac{c^2 \sigma_{\text{rcs},l}}{(4\pi)^3 f_c^2 d_l^4} \end{aligned} \quad (4)$$

where  $G_R$  represents the gain of a single antenna element at the Rx,  $\gamma_l = |\text{AF}(\theta_{T,s} - \theta_l)|^2 \in [0, 1]$  denotes the normalized array gain at the Tx, which considers the imperfect alignment between the sensing direction and the target DoA,  $N_0$  is the one-sided noise power spectral density (PSD) at Rx,  $d_l$  represents the distance between the  $l$ th reflection point and the BS,  $\sigma_{\text{rcs},l}$  corresponds to the RCS,  $f_c$  is the carrier frequency and  $c$  is the speed of light.

The RCSs  $\sigma_{\text{rcs},l}$  of scatterers for both pedestrians and vehicles are random and modeled according to a Swerling I type distribution whose mean value,  $\bar{\sigma}_{\text{rcs}}$ , can be found in Table I [14]. It is important to note that the number of backscattered signals  $L$  depends on the relative angular position with respect to the BS and varies over time according to a visibility function [11], as objects are moving.

### B. Measurement Model

As mentioned, each BS detects objects in the environment by scanning using a multi-beam pattern defined in Equation (1). Specifically, the communication beam is directed toward a UE, while the sensing direction changes over time, sequentially pointing toward various directions following a predefined angular increment. In each direction, a set of  $M_s$  OFDM symbols is collected to form the grid of received symbols  $\mathbf{Y}_s$ , which is then used to obtain a range-angle map. The period required to complete a full scan, denoted as  $T_{\text{scan}}$ ,

depends on the chosen number of sensing directions and on the symbol duration  $T_s$ . Once all the symbols are acquired and assembled into the matrix  $\mathbf{Y}_s$ , the first step involves an element-wise division between  $\mathbf{Y}_s$  and  $\mathbf{X}_s$ , an operation often indicated as reciprocal filtering [15], [16]. This division aims to eliminate the influence of the transmitted symbols and generate a new matrix denoted as  $\mathbf{G}_s$ . Subsequently, a double-periodogram is performed on the rows and columns of  $\mathbf{G}_s$  to obtain a range-Doppler map [15]. From this map, a range-angle map  $\mathbf{D}_{q,t}$  is derived at the  $q$ th BS and  $t$ th scan by selecting the column of the periodogram with the maximum value and uniquely associating it with the corresponding scan direction.<sup>2</sup>

### III. DATA FUSION, TARGET CLASSIFICATION, AND TARGET-ORIENTED PROCESSING

According to the block diagram depicted in Figure 2, each BS exchanges the range-angle map denoted as  $\mathbf{D}_{q,t}$  with the FC. The FC employs a linear uniform grid, with resolution  $\Delta_x$  and  $\Delta_y$  (with  $N_x$  and  $N_y$  points) as a baseline. The received maps are rotated and translated according to the specific BS position and ULA orientation, and resampled at the baseline grid to ensure consistent map fusion. Subsequently, the resampled range-angle maps, represented as  $\overline{\mathbf{D}}_{q,t}$ , are combined via element-wise summation to yield the soft map  $\mathbf{L}_t = \sum_{q=1}^{N_s} \overline{\mathbf{D}}_{q,t}$ , where  $N_s$  is the number of BSs performing sensing.<sup>3</sup>

#### A. Target Identification

Each target exhibits a different reflection pattern related to its geometrical shape and RCS, namely its reflection fingerprint. To this end, a convolutional neural network (CNN) is adopted to infer the target category (pedestrian or vehicle) directly from the resampled and fused soft maps  $\mathbf{L}_t$  which contain such information.

Following Figure 2, a first step named image cropping is required to isolate each target from the others. A square window with side  $W_{\text{size}}$  pixels is selected to frame each target. Such windows are centered in the predicted target position at time  $t$ , inferred by the tracking algorithms exploiting information extracted during the previous time step  $t - 1$ . To generate the training set for the CNN, we consider a scenario where actual target positions and categories are known. To increase the classifier performance and robustness in the presence of imperfect target state predictions, which result in a misalignment between targets and relative frames, during training, the real target position is perturbed, adding Gaussian noise (which acts as a random displacement) with standard deviation  $\sigma_w$  on both  $x$  and  $y$  directions. This solution leads to more accurate target classification, reducing the generalization error. At the end of the training phase, the CNN can infer the target category in real time and in a different scenario.

<sup>2</sup>The estimation of target parameters turns out to be a frequency estimation problem; hence, since the periodogram represents (asymptotically) the log-likelihood, the column with the maximum value is selected.

<sup>3</sup>Since  $\mathbf{L}_t$  are obtained via periodogram estimation, they can be interpreted as target log-likelihood maps, hence their summation results from noise independence among BS.

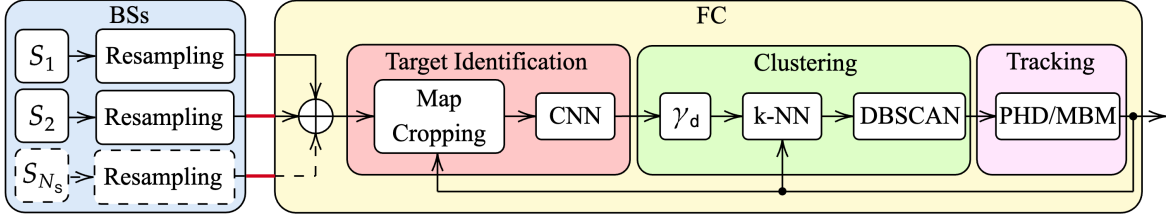


Figure 2: Block diagram of the sensing processing chain exploiting BS cooperation, target classification, and target-specific tracking. The BSs scan the environment generating range-angle maps and resample them according to a predefined grid. Resampled range-angle maps are then shared with the FC and fused in a single map. Target identification is performed at the FC through map cropping and classification (red block). Then clustering is performed to merge detections generated by the same target (green block). Finally, tracking algorithms perform target state estimation (pink block).

### B. Adaptive Clustering

A three-step clustering procedure is employed to extract detections from the soft maps, enabling effective handling of extended and point-like objects (refer to Figure 2 green block for a visual representation of the clustering procedure). The main steps of the proposed strategy can be summarized as follows:

- 1) An excision filter is implemented with threshold  $\gamma_d$ , to remove points with low values from the  $\mathbf{L}_t$  maps which are likely produced by noise.
- 2) A k-nearest neighbors (k-NN) algorithm with  $k = 1$  and adaptive gate  $\xi_k$  (to ignore residual points distant from each target) are applied to cluster data that likely belong to a previously detected target [17]. It is important to highlight that the parameter  $\xi_k$  can be adapted and varied depending on the target category. Section IV compares the solution with fixed values of  $\xi_k$  and the adaptive solution.
- 3) The remaining points (i.e., map points larger than  $\gamma_d$  and outside the gate  $\xi_k$ ) are clustered through the density-based spatial clustering of applications with noise (DBSCAN) algorithm, with a maximum distance between points belonging to the same cluster  $\xi_d$ , and a minimum number of points to form a cluster  $N_d$  [18].

Finally, each cluster centroid is stored in the matrix  $\mathbf{Z}_t$ , representing target detections extracted from the soft maps.

### C. Tracking Algorithms

For all the tracking algorithms, we adopt the following state vector to represent the state of each target

$$\mathbf{s}_{t,n} = (s_{t,n,x}, s_{t,n,y}, s_{t,n,v_x}, s_{t,n,v_y})^T \quad (5)$$

where  $t$  and  $n$  are the time and target indexes. The first two elements of the vector correspond to the target position coordinates, while the last two represent the target velocity components. To update the target position coordinates, we use the information extracted from the map, while the target velocity components are inferred by considering both the previous target position at time  $t - 1$  and the current target position.

The PHD filter is a widely adopted algorithm in literature [19], [20]. One possible implementation suggests approximating the target intensity function as a Gaussian mixture (GM)

with a predefined number of components, which takes the following form

$$D_{t-1|t-1}(\mathbf{x}) = \sum_{h=1}^{\mathcal{H}_{t-1|t-1}} w_{t-1|t-1}^{(h)} \mathcal{N}_{\mathbf{x}}(\boldsymbol{\mu}_{t-1|t-1}^{(h)}, \mathbf{P}_{t-1|t-1}^{(h)}) \quad (6)$$

where  $\mathbf{x}$  is a generic random finite set (RFS),  $\mathcal{H}_{t-1|t-1}$  represents the number of Gaussian components in the intensity function,  $w_{t-1|t-1}^{(h)}$  is the  $h$ th component weight, and  $\boldsymbol{\mu}_{t-1|t-1}^{(h)}$  and  $\mathbf{P}_{t-1|t-1}^{(h)}$  represent mean and covariance of the considered component. The intensity function can be interpreted as an atypical probability density function (p.d.f.) whose integral returns the estimated number of targets in the scenario.

The prediction step infers the intensity function in the consecutive time step, i.e.,  $D_{t|t-1}(\mathbf{x})$ , through a linear Kalman predictor [21]. During prediction, the probability of survival  $P_s$  is considered constant, so are the transition matrix  $\mathbf{F}$  and the process noise covariance matrix  $\mathbf{Q}$ ; the last one represents the motion uncertainty. A set of  $\mathcal{B}$  birth components is added to the predicted intensity function  $D_{t|t-1}(\mathbf{x})$  to represent the possibility of new targets spawning in the surveillance area. The total number of components after prediction is then  $\mathcal{H}_{t|t-1} = \mathcal{H}_{t-1|t-1} + \mathcal{B}$ .

In the update step, the predicted components are updated through the Kalman update equations, as in [21], with the measurements  $\mathbf{Z}_t$  extracted from the maps  $\mathbf{L}_t$ . During this step, the detection probability  $P_d$  is considered constant, and the covariance matrix  $\mathbf{R}_t$  for each measurement is estimated from the selected map detection points, as will be highlighted in Equation (15). The overall amount of components in the posterior can be written as  $\mathcal{H}_{t|t} = \mathcal{H}_{t|t-1}(M_t + 1)$ , where  $M_t$  denotes the number of measurements at time instant  $t$ .

To estimate the number of targets from the PHD posterior, it is enough to sum the weight of the components and round it to the closest integer

$$\hat{N}_{\text{obj}} = \left\lfloor \sum_{h=1}^{\mathcal{H}_{t|t}} w_{t|t}^{(h)} \right\rfloor \quad (7)$$

while for the  $n$ th target state estimation, we extract the mean value of the  $n$ th most likely component

$$\hat{\mathbf{s}}_{t,n} = \underset{w_{t|t}^{(h)}}{\operatorname{argmax}} \boldsymbol{\mu}_{t|t}^{(h)} \quad (8)$$

The MBM filter is an alternative to the PHD filter for multiple target tracking problems that exploit the association probability between measurements and targets [22], [23]. The MBM filter is used to approximate the target multi-object p.d.f.

$$\text{MBM}_{t-1|t-1}(\mathbf{x}) = \sum_{g=1}^{\mathcal{G}_{t-1|t-1}} w_{t-1|t-1}^{(g)} \text{MB}_{t-1|t-1}^{(g)}(\mathbf{x}) \quad (9)$$

where  $\mathcal{G}_{t-1|t-1}$  represents the number of multi-Bernoulli (MB) components or global hypothesis in the MBM distribution, and  $w_{t-1|t-1}^{(g)}$  stands for the  $g$ th MBM component weight. The MB distribution in Equation (9) can be written as follows

$$\text{MB}_{t-1|t-1}^{(g)}(\mathbf{x}) = \sum_{\mathfrak{U} \ni \mathbf{x}_l = \mathbf{x}} \prod_{l=1}^{\mathcal{L}_{t-1|t-1}^{(g)}} \text{B}_{t-1|t-1}^{(g,l)}(\mathbf{x}_l) \quad (10)$$

where  $\mathcal{L}_{t-1|t-1}^{(g)}$  represents the number of Bernoulli components or local hypothesis in the MB distribution, and the summation is performed for all the possible unions of mutually disjoint RFS that generate  $\mathbf{x}$ , which means to evaluate all the possible data associations between measurements and targets [23]. The single Bernoulli component in Equation (10) can be written as

$$\text{B}_{t-1|t-1}^{(g,l)}(\mathbf{x}_l) = r_{t-1|t-1}^{(g,l)} \mathcal{N}_{\mathbf{x}_l}(\boldsymbol{\mu}_{t-1|t-1}^{(g,l)}, \mathbf{P}_{t-1|t-1}^{(g,l)}) \quad (11)$$

where  $r_{t-1|t-1}^{(g,l)}$  represents the existence probability of the  $l$ th local hypothesis in the  $g$ th global hypothesis,  $\boldsymbol{\mu}_{t-1|t-1}^{(h)}$  and  $\mathbf{P}_{t-1|t-1}^{(h)}$  represent the mean and the covariance of the considered component, respectively.

During prediction, linear Kalman prediction is performed again to infer the parameters in the consecutive time step. To account for new spawning objects, a set of  $\mathcal{B}$  Bernoulli components is added to each global hypothesis. For both algorithms, to exploit the prior information about the environment, the components are generated following the scenario layout, i.e., the number of hypotheses, their mean value, covariance, and weight are based on the lanes and crosswalk positions in the environment. The overall number of components after the prediction step can be evaluated as  $(\mathcal{L}_{t-1|t-1} + \mathcal{B})\mathcal{G}_{t-1|t-1}$ .

In the update phase, a linear Kalman update is performed to derive the updated parameters, considering the most likely association between measurements and targets [22]. Estimations  $\hat{\mathbf{s}}_{t,n}$  are then extracted from the posterior distribution, considering the mean value  $\boldsymbol{\mu}_{t|t}^{(i,j)}$  of the MB components with existence probability  $r_{t|t}^{(i,j)} \geq \gamma_e$  from the MBM component with highest probability  $w_{t|t}^{(i)}$ .

#### D. Motion and Measurement Model

To model clutter measurements representing false alarm detection extracted by the clustering procedure, a Poisson point process (PPP) is considered, whose intensity is defined as  $\lambda_c$ .

Target death is modeled through a constant probability of survival  $P_s$ . During prediction, if a component is associated with a missed detection, its weight is multiplied by a factor proportional to  $P_s$ , which means that consecutive missed detections lead to unlikely target state components.

A linear prediction model is selected to track the behavior of both extended and point-like targets. This is justified by the low value of  $T_{\text{scan}}$  compared to the target velocity, which allows to approximate target motions as piecewise linear among consecutive acquisitions. The corresponding transition matrix and process noise covariance matrix are

$$\mathbf{F} = \begin{bmatrix} 1 & 0 & T_{\text{scan}} & 0 \\ 0 & 1 & 0 & T_{\text{scan}} \\ 0 & 0 & 1 & 0 \\ 0 & 0 & 0 & 1 \end{bmatrix} \quad (12)$$

$$\mathbf{Q} = \alpha_q T_{\text{scan}} \cdot \mathbf{I}_4 \quad (13)$$

where  $\alpha_q$  is a parameter that represents the prediction uncertainty about the target motion.

In this work, only position information about the targets is estimated through measurements, while consecutive position measurements are used to infer the velocity.<sup>4</sup> With these assumptions, the following measurement matrix is considered

$$\mathbf{H} = \begin{bmatrix} 1 & 0 & 0 & 0 \\ 0 & 1 & 0 & 0 \end{bmatrix}. \quad (14)$$

Because of the high-resolution maps, multiple detections (closely spaced map pixels) from each target are generated, leading to a non-diagonal measurement covariance matrix. Thus such a matrix needs to be estimated. Let us define the set of map points  $\mathbf{L}_t^{(\mathbf{z}_{t,m})}$  extracted after clustering, specified by  $\mathbf{z}_{t,m}$ , from the measurement matrix (map)  $\mathbf{L}_t$ . Indicating with  $\mathbf{V}_t^{(\mathbf{z}_{t,m})}$ , the  $2 \times N_{\mathbf{z}_{t,m}}$  matrix containing the pixel coordinates relative to  $\mathbf{L}_t^{(\mathbf{z}_{t,m})}$ , the sample covariance measurement matrix can be calculated as

$$\mathbf{R}_t = \frac{1}{N_{\mathbf{z}_{t,m}} - 1} \sum_{p=1}^{N_{\mathbf{z}_{t,m}}} (\mathbf{v}_{t,p}^{(\mathbf{z}_{t,m})} - \mathbf{z}_{t,m})(\mathbf{v}_{t,p}^{(\mathbf{z}_{t,m})} - \mathbf{z}_{t,m})^T \quad (15)$$

where  $N_{\mathbf{z}_{t,m}}$  represents the number of map points associated to the  $m$ th measurement  $\mathbf{z}_{t,m}$ , and  $\mathbf{v}_{t,p}^{(\mathbf{z}_{t,m})}$  stands for the  $p$ th map point coordinates in the matrix  $\mathbf{V}_t^{(\mathbf{z}_{t,m})}$ .

#### E. Post-Processing

A set of post-processing procedures are implemented to manage the complexity of the algorithms and ensure good estimation accuracy. In the PHD filter, pruning, capping, and merging are implemented sequentially to reduce the number of components in the posterior intensity function. Pruning removes all the components in the posterior whose weights  $w_{t|t}^{(h)}$  are under a predefined threshold  $\gamma_p$  [20]. Then, capping is realized on the remaining components selecting the  $\gamma_q$  components with the greatest  $w_{t|t}^{(h)}$ , by fixing the maximum number of components in the posterior to  $\gamma_q$  [22].

Finally, on the remaining components in the set  $\zeta_m$ , merging of those whose average distance, defined in the following equation, is lower than a predefined threshold  $\gamma_s$  is performed:

$$d(\boldsymbol{\mu}_{t|t}^{(i)}, \boldsymbol{\mu}_{t|t}^{(j)}) = \|\boldsymbol{\mu}_{t|t}^{(i)} - \boldsymbol{\mu}_{t|t}^{(j)}\|_2 \quad (16)$$

<sup>4</sup>Although possible we consider the BS do not estimate target Doppler.

where weights, mean, and covariance are updated as follows:

$$\begin{aligned} w_{t|t}^{(k)} &= \sum_{i \in \zeta_m} w_{t|t}^{(i)} \\ \boldsymbol{\mu}_{t|t}^{(k)} &= \sum_{i \in \zeta_m} w_{t|t}^{(i)} \boldsymbol{\mu}_{t|t}^{(i)} \\ \mathbf{P}_{t|t}^{(k)} &= \sum_{i \in \zeta_m} w_{t|t}^{(i)} \mathbf{P}_{t|t}^{(i)} + (\boldsymbol{\mu}_{t|t}^{(i)} - \boldsymbol{\mu}_{t|t}^{(k)})(\boldsymbol{\mu}_{t|t}^{(i)} - \boldsymbol{\mu}_{t|t}^{(k)})^T \end{aligned}$$

where  $k$  represents the new index assigned to the derived component, and  $i$  represents the index of the merged component.

In the MBM filter, during the update phase, a gate for eligible data association allows pruning all the weak association hypotheses with  $w_{t|t}^{(k)} < \xi_a$ . Both the MBM and the MB components are pruned with the threshold  $\gamma_g$  and  $\gamma_l$ , respectively. Then, the residual MBM components are capped with a threshold  $\gamma_c$ . To increase the estimation accuracy, in the most likely MBM components, the MB components closer than  $\gamma_m$  are merged as previously described.

## IV. NUMERICAL RESULTS

### A. Performance Metrics

From the communication perspective, the aggregate network capacity, intended as the sum rate of each BS in the downlink, is considered to assess the communication performance. Considering  $N_s$  BSs dedicated for both sensing and communications among the  $N_{\text{tot}}$  available BSs (so  $N_{\text{tot}} - N_s$  are for communication only) and a fraction of power dedicated for sensing  $\rho_p$  (1), the overall aggregate network capacity can be written as

$$\begin{aligned} C(\rho_p) &= (N_s \Delta f K \log_2(1 + (1 - \rho_p) \text{SNR}^{(c)}) \\ &+ (N_{\text{tot}} - N_s) \Delta f K \log_2(1 + \text{SNR}^{(c)})) / N_{\text{tot}} \end{aligned} \quad (17)$$

where  $\text{SNR}^{(c)}$  is the communication SNR experienced by the users.<sup>5</sup>

To evaluate the network localization capability, the OSPA is selected as a single-value metric [?], [?]

$$\text{OSPA} = \sqrt[p]{\frac{1}{N_c} \left( \sum_{(i,j) \in \zeta_g^*} d(\hat{\mathbf{s}}_{t,i}, \hat{\mathbf{s}}_{t,j})^p + \frac{\xi_g^p}{2} (|\mathbf{S}_t| + |\hat{\mathbf{S}}_t| - 2|\zeta_g^*|) \right)}$$

where  $\hat{\mathbf{S}}_t$  contains the position coordinates for all the estimated targets in the scenario representing the first two rows of  $\hat{\mathbf{S}}_t$  inferred by the algorithms, and  $N_c$  is the number of elements in the OSPA metric given by  $N_c = |\mathbf{S}_t| + |\hat{\mathbf{S}}_t| - |\zeta_g^*|$ , where  $|\cdot|$  represents the RFS cardinality. The parameter  $p$  is the OSPA order, while  $\xi_g$  represents the OSPA gate. Estimations beyond the gate threshold  $\xi_g$  are categorized as false alarms, while actual target positions not linked to estimations within the gate are classified as missed detections. The set  $\zeta_g^*$  represents the best assignment between the estimated set of objects  $\hat{\mathbf{S}}_t$  and the ground truth one  $\mathbf{S}_t$ . The best assignment is selected as the one that minimizes the OSPA error. Note that the first term in

the OSPA metric, i.e.,  $d(\hat{\mathbf{s}}_{t,i}, \hat{\mathbf{s}}_{t,j})^p$ , can be interpreted as the distance between the estimated target positions and the real ones (and if  $p = 2$ , this term corresponds to the square error of position estimation). The rest of the OSPA metric can be rewritten as

$$\frac{\xi_g^p}{2} (|\mathbf{S}_t| - |\zeta_g^*|) + \frac{\xi_g^p}{2} (|\hat{\mathbf{S}}_t| - |\zeta_g^*|) \quad (18)$$

where the first term is proportional to the missed detections, while the second term is related to the false alarms.

Finally, to evaluate the target classification performance, we define the classification accuracy as

$$\text{Accuracy} = \frac{T_P + T_N}{T_P + T_N + F_P + F_N} \quad (19)$$

where  $T_P$ ,  $T_N$ ,  $F_P$ , and  $F_N$  stand for true positive, true negative, false positive, and false negative classifications, respectively.

### B. Parameter Setup

We considered a scenario with  $N_{\text{tot}} = 6$  BSs, and a set of 4 extended and 4 point-like targets. Pedestrians and vehicles move as a mix of constant turns, linear accelerated/decelerated, static, and uniform linear motions. The area monitored is of size  $x \in [-20, 20]$  m and  $y \in [-20, 20]$  m. The BSs are positioned on a circumference of radius 50 m centered in the surveillance area, with the axes normal to the ULAs pointing toward the center, a scanning aperture of  $120^\circ$  (i.e.,  $\Theta_0 = 60^\circ$ ), and scan step  $\Delta\Theta = 2.4^\circ$ .

The transmission parameters are: quadrature phase shift keying (QPSK) modulation,  $f_c = 28$  GHz,  $\Delta f = 120$  kHz,  $K = 3168$  (i.e., about 400 MHz bandwidth),  $M = 1120$ , and  $M_s = 112$ . The effective isotropic radiated power (EIRP) is set to 30 dBm, and the noise PSD is  $N_0 = 4 \cdot 10^{-20}$  W/Hz. All the 6 BSs are equipped with  $N_T = N_R = 50$  antennas. At each BS, the scan duration is  $T_{\text{scan}} = 50$  ms, and the overall scenario is monitored for 10 s, resulting in  $N_m = 200$  measurements (maps collected). The grid resolution for map fusion is set to  $\Delta_x = 0.1$  m and  $\Delta_y = 0.1$  m. The fraction of power dedicated to sensing  $\rho_p$  is set to 0.3; the same for all BSs.

For the target identification task, the window size is set to  $W_{\text{size}} = 6$  m, and the position perturbation standard deviation is  $\sigma_w = 0.5$  m. The CNN is composed of a 2D convolutional layer with 20 random mask filters of dimension  $5 \times 5$  and rectified linear unit (ReLU) activation function, a consecutive 2D max pooling layer which performs a down-sampling of a factor 2, and a fully connected layer with the softmax activation function whose output dimension is 2, to map the extracted features in the target classes.

In the clustering algorithm, the detection threshold is set to  $\gamma_d = 2 \cdot 10^{-7}$ . The k-NN gate  $\xi_k$  is tested for values between 4 and 6. For DBSCAN, the cutoff distance is  $\xi_d = 3$ , and the minimum number of points to form clusters is set to  $N_d = 50$ .

In both tracking algorithms, the clutter intensity is  $\lambda_c = 0.1$ , the prediction uncertainty is  $\alpha_q = 5$ , and the initial component covariance is set to  $\mathbf{P} = 0.5 \cdot \mathbf{I}_4$ . The probabilities of detection and survival are  $P_d = 0.99$  and  $P_s = 0.9$ , respectively. The

<sup>5</sup>To keep the presentation of numerical results simple, we consider all the UEs experience the same SNR.

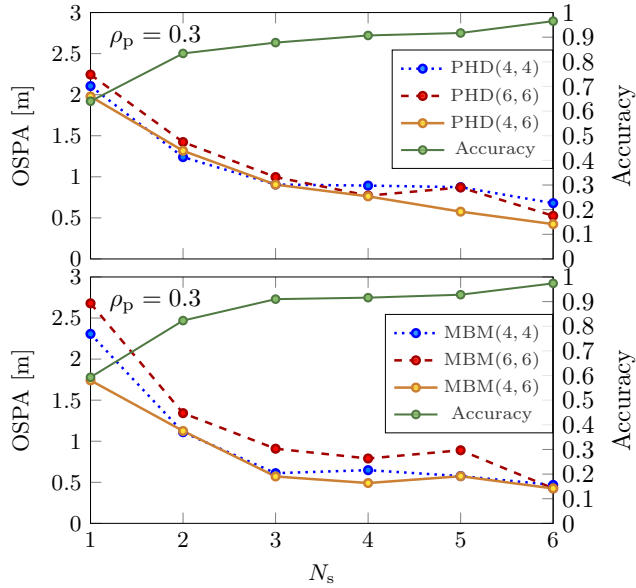


Figure 3: Localization performance and classification accuracy varying the number of BSs devoted for sensing  $N_s$  for the PHD (top) and MBM (bottom)

merging threshold is set to  $\gamma_m = 5$ . In the PHD filter, the pruning threshold of the components is  $\gamma_p = 100 \cdot 10^{-6}$ , while the maximum number of components is fixed to  $\gamma_q = 10$ . In the MBM filter, the pruning threshold on the probability of existence is  $\gamma_l = 100 \cdot 10^{-6}$  while the pruning threshold on the MBM components is set to  $\gamma_g = 10^{-15}$ . The maximum number of MBM components is  $\gamma_c = 10$ . The gate for the admissible associations is set to  $\xi_a = 14$ . The existing threshold is  $\gamma_e = 0.99$ . For both the algorithms, the birth components for new appearing objects are initialized with covariance  $\mathbf{P}^{(b)} = 0.1 \cdot \mathbf{I}_4$ , with position  $\boldsymbol{\mu}^{(b)}$  reflecting the possible target spawn position. A recovery component is initialized centered in the scenario with covariance  $\mathbf{P}^{(b)} = 5 \cdot \mathbf{I}_4$ .

### C. Target Classification Performance

In Figure 3, the classification accuracy for  $\rho_p = 0.3$ , and varying the number of BSs selected for sensing  $N_s$ , is reported in green for both PHD and MBM, on the top and bottom plots, respectively. It can be noticed that both the algorithms ensure a target classification accuracy greater than 0.85 when the number of BSs is  $N_s \geq 3$ . Classification performance is highly influenced by the number of BSs adopted for sensing; reducing the number of BSs reduces the number of detected reflection points of extended targets (because of the reduction of spatial diversity), resulting in more similar target fingerprints between pedestrians and vehicles in the fused maps. It is also interesting to notice that with  $N_s = 6$  BSs, the target classification accuracy is greater than 98%, representing a remarkable result.

### D. Sensing and Communication Performance

In Figure 3, the OSPA metric for  $\rho_p = 0.3$ , and varying the number of sensors  $N_s$ , is illustrated for PHD and MBM, on the top and bottom, respectively. Blue dotted curves represent

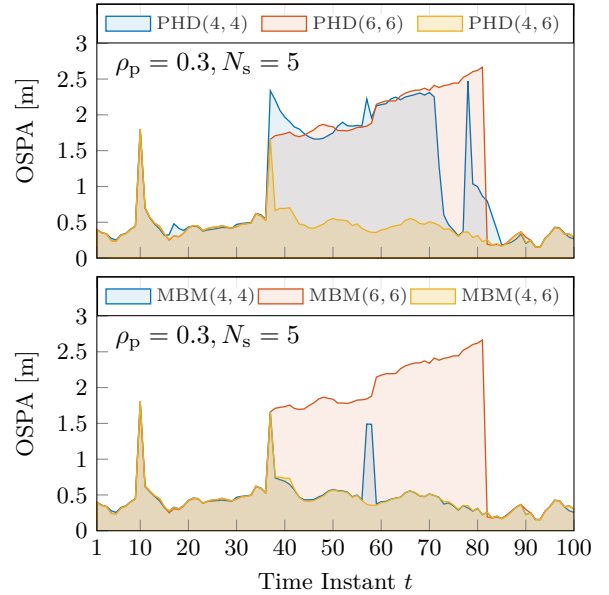


Figure 4: Localization performance over time for the PHD (top) and MBM (bottom)

the algorithm performance with  $\xi_k = 4$  for both pedestrians and vehicles; red dashed curves refer to the performance with  $\xi_k = 6$  again for both pedestrians and vehicles. Solid yellow curves represent the performance of the AI-based solution, whose gates are adapted for pedestrians ( $\xi_k = 4$ ) and vehicles ( $\xi_k = 6$ ) based on the target identification.

As can be noticed, the adaptive gate achieves a lower localization error for both algorithms. For the PHD filter, the solution with adaptive gating presents an error lower than 1 m when the number of sensors is  $N_s \geq 3$ . Similarly, the MBM filter exhibits an OSPA lower than 0.7 m considering  $N_s \geq 3$ . The performance degradation experienced when  $N_s < 3$  is due to target misclassification. In this case, the adaptive solution is affected by the mismatch between the real target classes and the estimated ones, resulting in an incorrect assignment of the gating parameter  $\xi_k$ .

To emphasize the benefit produced by the adoption of adaptive gating (see Figure 4), the number of BSs devoted to sensing is fixed. At the same time, the OSPA metric is reported over the first 100 acquisitions. Blue areas represent the OSPA produced by a fixed gate  $\xi_k = 4$  for both pedestrians and vehicles, red areas refer to the solution with  $\xi_k = 6$ , and yellow areas represent the adaptive solution. It is important to highlight the increase in the localization performance thanks to adaptive gating for both algorithms, which results in reduced OSPA peaks.

From a communication perspective, the BS aggregate capacity is evaluated with Equation (17), considering  $\rho_p = 0.3$ . The worst case for communication is when all the BSs are performing joint communication and sensing, i.e.,  $N_s = 6$ . In this situation, the downlink capacity is  $C = 0.9$  Gbit/s. On the contrary, without performing sensing ( $N_s = 0$ ), the downlink capacity can reach  $C = 1.1$  Gbit/s. As a compromise, using 3 BSs for JSC and 3 for communication only, the downlink

capacity can be maintained greater than  $C = 1$  Gbit/s.

## V. CONCLUSION

In this work, we presented a framework to perform JSC with OFDM waveforms exploiting cooperation and data fusion among BSs to improve localization performance. Furthermore, leveraging different target reflection fingerprints in the soft maps, we developed a CNN classifier to identify the object type and adapt the multi-target tracking to the specific object type.

A three-step clustering strategy based on adaptive gating is proposed to manage point-like and extended targets and exploit target identification. Then, two multi-target tracking algorithms are used, the PHD and MBM filters, to track all the targets in the surveillance area.

The overall system is tested in a vehicular scenario with two types of targets, pedestrians and vehicles. To explore the communication/sensing trade-off, we investigated the sensing performance varying the number of cooperating BSs, considering that a fraction of transmit power is devoted to the sensing beams.

The system performance has been evaluated through the OSPA metric, target classification accuracy, and communication performance via aggregate downlink capacity. Numerical results show that adaptive gating aided by target identification performs better than the simpler target-agnostic solution when the target classification accuracy is greater than 90%. For example, by choosing  $N_s = 3$  BSs, a classification accuracy around 0.9 is reached, with an OSPA error lower than 1 m for the PHD filter and around 0.7 m for the MBM filter, while also ensuring a downlink capacity greater than 1 Gbit/s. With  $N_s = 6$  sensing BSs, a target classification accuracy larger than 98% is reached, with a localization error lower than 0.7 m for both tracking algorithms, with a penalty on downlink capacity of 10%, i.e., from 1 Gbit/s to 0.9 Gbit/s.

## REFERENCES

- [1] R. Thomä, T. Dallmann, S. Jovanoska, P. Knott, and A. Schmeink, "Joint communication and radar sensing: An overview," in *Europ. Conf. on Ant. and Prop. (EuCAP)*, Dusseldorf, Germany, Mar. 2021, pp. 1–5.
- [2] S. Schieler, C. Schneider, C. Andrich, M. Döbereiner, J. Luo, A. Schwind, R. S. Thomä, and G. Del Galdo, "OFDM waveform for distributed radar sensing in automotive scenarios," *Int. J. of Microw. and Wireless Tech.*, vol. 12, no. 8, p. 716–722, 2020.
- [3] J. Zhang, X. Wang, P. Liu, J. Huang, and Z. Zheng, "Joint resource allocation and user association for multi-cell integrated sensing and communication systems," *EURASIP Journal on Wireless Communications and Networking*, vol. 2023, 07 2023.
- [4] Z. Wang, K. Han, J. Jiang, F. Liu, and W. Yuan, "Multi-vehicle tracking and ID association based on integrated sensing and communication signaling," *IEEE Wireless Commun. Letters*, vol. 11, no. 9, pp. 1960–1964, 2022.
- [5] J. A. Zhang, F. Liu, C. Masouros, R. W. Heath, Z. Feng, L. Zheng, and A. Petropulu, "An overview of signal processing techniques for joint communication and radar sensing," *IEEE J. of Sel. Topics in Signal Process.*, vol. 15, no. 6, pp. 1295–1315, 2021.
- [6] Y. Cui, F. Liu, X. Jing, and J. Mu, "Integrating sensing and communications for ubiquitous IoT: Applications, trends, and challenges," *IEEE Netw.*, vol. 35, pp. 158–167, 2021.
- [7] R. Liu, M. Jian, D. Chen, X. Lin, Y. Cheng, W. Cheng, and S. Chen, "Integrated sensing and communication based outdoor multi-target detection, tracking and localization in practical 5G networks," *arXiv preprint arXiv:2305.13924*, 2023.
- [8] R. Chauhan, K. K. Ghanshala, and R. Joshi, "Convolutional neural network (CNN) for image detection and recognition," in *2018 1th Int. Conf. on Secure Cyber Comput. and Commun. (ICSCCC)*, 2018, pp. 278–282.
- [9] O. Kechagias-Stamatis and N. Aouf, "Automatic target recognition on synthetic aperture radar imagery: A survey," *IEEE Aerosp. Electron. Syst. Mag.*, vol. 36, no. 3, pp. 56–81, 2021.
- [10] Y. Tian, "Artificial intelligence image recognition method based on convolutional neural network algorithm," *IEEE Access*, vol. 8, pp. 125 731–125 744, 2020.
- [11] M. Bühren and B. Yang, "Simulation of automotive radar target lists using a novel approach of object representation," in *IEEE Intell. Veh. Symp.*, 2006, pp. 314–319.
- [12] E. Favarelli, E. Matricardi, L. Pucci, E. Paolini, W. Xu, and A. Giorgetti, "Sensor fusion and extended multi-target tracking in joint sensing and communication networks," in *IEEE Int. Conf. on Commun. (ICC)*, accepted, Rome, Italy, May 2023.
- [13] —, "Map fusion and heterogeneous objects tracking in joint sensing and communication networks," in *20th European Radar Conference (EuRAD)*, accepted, Berlin, Germany, Sep. 2023.
- [14] M. I. Skolnik, *Radar handbook*. McGraw-Hill Education, 2008.
- [15] L. Pucci, E. Paolini, and A. Giorgetti, "System-level analysis of joint sensing and communication based on 5G new radio," in *IEEE J. Sel. Areas Commun.*, vol. 40, no. 7, July 2022, pp. 2043–2055.
- [16] J. T. Rodriguez, F. Colone, and P. Lombardo, "Supervised reciprocal filter for ofdm radar signal processing," *IEEE Transactions on Aerospace and Electronic Systems*, pp. 1–22, 2023.
- [17] J. Watt, R. Borhani, and A. K. Katsaggelos, *Machine Learning Refined*. Cambridge University Press, 2016.
- [18] M. Ester, H.-P. Kriegel, J. Sander, and X. Xu, "A density-based algorithm for discovering clusters in large spatial databases with noise," in *Int. Conf. on Know. Disc. in Data Mining*, Portland, Oregon, 1996, pp. 226–231.
- [19] R. Mahler, "PHD filters of higher order in target number," *IEEE Trans. Aerosp. Electron. Syst.*, vol. 43, no. 4, pp. 1523–1543, 2007.
- [20] B.-N. Vo and W.-K. Ma, "The Gaussian mixture probability hypothesis density filter," *IEEE Trans. Signal Process.*, vol. 54, no. 11, pp. 4091–4104, 2006.
- [21] Q. Li, R. Li, K. Ji, and W. Dai, "Kalman filter and its application," in *8th International Conference on Intell. Networks and Intell. Systems (ICINIS)*, 2015, pp. 74–77.
- [22] A. F. García-Fernández, Y. Xia, K. Granström, L. Svensson, and J. L. Williams, "Gaussian implementation of the multi-Bernoulli mixture filter," in *22th Int. Conf. on Inf. Fusion (FUSION)*, 2019, pp. 1–8.
- [23] A. F. García-Fernández, J. L. Williams, K. Granström, and L. Svensson, "Poisson multi-bernoulli mixture filter: Direct derivation and implementation," *IEEE Trans. on Aerosp. Electron. Syst.*, vol. 54, no. 4, pp. 1883–1901, 2018.